Hot nanoindentation in inert environments

Jonathan C. Trenkle, Corinne E. Packard, and Christopher A. Schuh
Department of Materials Science and Engineering, Massachusetts Institute of Technology, Cambridge, Massachusetts 02139

Abstract

An instrument capable of performing nanoindentation at temperatures up to 500°C in inert atmospheres, including partial vacuum and gas near atmospheric pressures, is described. Technical issues associated with the technique (such as drift and noise) and the instrument (such as tip erosion and radiative heating of the transducer) are identified and addressed. Based on these considerations, preferred operation conditions are identified for testing on various materials. As a proof-of-concept demonstration, the hardness and elastic modulus of three materials are measured: fused silica (non-oxidizing), aluminum and copper (both oxidizing). In all cases, the properties match reasonably well with published data acquired by more conventional test methods.

1 Introduction

Over the past two decades, instrumented nanoindentation has become a ubiquitous technique for obtaining reliable mechanical property measurements from microscale amounts of material, including thin films, single grains, and individual phases of composites [1]. Furthermore, because of its high sensitivity, nanoindentation can be a powerful tool to probe physical phenomena in materials, such as dislocation nucleation [2-4], shear band activation [5-6] and phase transformations [7-9]. For all of these purposes, however, nanoindentation testing has most commonly been conducted at room temperature. This is in spite of the fact that micro-materials and devices are often employed at elevated temperatures, and deformation physics are usually thermally activated.

While "hot hardness" testing has been used on macro-scales for many decades, it is only more recently that nanoindentation has been performed at elevated temperatures. Figure 1 is a graphical summary of various experiments reported in the literature [3, 5, 8, 10-47], which logs the test temperature and characteristic scale of the indentations for each study. (Note that in this figure that micro- and nano-indentations are differentiated by symbol). The points in Figure 1 define an envelope that reflects the current "state of the art" in high temperature indentation; all combinations of temperature and depth within the envelope can be accessed with reasonable experimental resolution. However, if this envelope is further segmented according to the materials tested, we can identify a much smaller region that is accessible to oxidizing materials such as metals. In the existing experimental literature, studies on these materials either require a sufficiently low test temperature to retard oxide growth [3, 18, 22], or involve flowing inert gas to

dilute oxygen content in the atmosphere around the sample [48-49]. Avoiding oxidation is clearly a critical point for the smallest nanoindentation experiments, lest the measured properties become convoluted with those of the oxide. This concern becomes acute when studying physical phenomena, such as dislocation nucleation, that are best probed at very shallow indentation depths.

Besides oxidation, a second major issue in elevated temperature nanoindentation is thermal drift. Thermal drift occurs when any component in the load frame expands or contracts in response to changing thermal gradients, resulting in the measurement of apparent displacement that is not a true reflection of a material's force-displacement response. During testing at room temperature, thermal drift is generally low and assumed to be constant throughout the test, allowing it to be subtracted from the material response in a straightforward manner. With the addition of a heat source, there is potential for larger thermal gradients and fluctuations in the load frame, thus leading to higher drift rates, increased variation in drift rate from one nanoindentation to the next, and even a progression of drift rate over the duration of a single test. A previous report from our group [33] showed that thermal drift can be adequately managed during testing in air up to 400°C with appropriate equilibration; however, the trend of increasing thermal drift rate with temperature observed there raised concerns for the viability of high quality testing at higher temperatures. Universally achieving nano-scale indentations at higher temperatures (and thus expanding the envelopes in Figure 1), requires instrumentation advances in two arenas: 1) minimizing or eliminating oxidation and 2) successful management of thermal drift and noise [47]. Oxidation is most effectively minimized by testing either in a vacuum or a controlled atmosphere. However, the introduction of a vacuum or inert gas inevitably changes thermal

transport in the system, and thus can impact thermal drift and noise during testing as well.

In the present work we report the development of a new instrument to perform hot nanoindentation experiments in a partial vacuum as well as in controlled atmospheres at near atmospheric pressures. We identify technical issues associated with testing in such environments, which can lead to significantly erroneous results if not properly monitored and managed. We also explore various configurations of the system, including different indenter tip architectures, to establish best practice techniques for high temperature nanoindentation in inert environments. As a proof-of-concept, we measure the hardness and modulus of three materials: fused silica (non-oxidizing), aluminum and copper (both oxidizing), to demonstrate that materials properties can be reliably extracted from high temperature nanoindentation tests.

2 Instrumentation

The basic nanoindenter platform that we use in this work is a Ubi1 from Hysitron, Inc. (Minneapolis, MN) with some proprietary modifications to enable its operation in a vacuum environment. We customize this instrument with a heating cartridge, a circulating cooling system, an actively cooled reflective shield, and a vacuum/atmosphere enclosure; the general arrangement of these components is shown schematically in Figure 2. In the Ubi1 system, the tip, force transducer, and piezo-electric fine positioning tube are oriented vertically in a compact design. Because all of the sensitive components are in close proximity (< 2 cm) to the heated sample, they must be thermally protected by the reflective shield, which is actively cooled by recirculating coolant at ~10^{o}C. The indenter shaft passes through a 4 mm diameter hole in the center of the shield to make contact with the sample. A J-type thermocouple is used to monitor

the temperature behind the shield, close to the indenter shaft. Even at sample temperatures above 500^{o} C, the temperature on the transducer side of the shield is maintained at or below room temperature.

The heating cartridge resembles a top hat (Figure 2B) and is made of copper with Ni-Cr resistance wire potted on the inside and wrapped around the outside of the copper shell. The cartridge sits on a tripod of three alumina balls (3 mm in diameter) on an actively cooled steel plate attached to an XY translation stage. The alumina ball mount provides a balanced mechanical support of reasonable stiffness, while minimizing heat conduction to the stage below. The heating cartridge is clamped to the stage using a steel collar with a ceramic washer placed between the collar and heater to minimize heat losses. Note that the design in Figure 2B thermally isolates the heating cartridge from the stage and load frame, as conductive paths for heat are limited and traverse low thermal conductivity ceramics.

We achieve inert atmospheres during testing by placing the entire nanoindentation system, including a passive vibration dampening stage (Minus K Technology, Inglewood, CA) into a custom-designed vacuum/inert atmosphere chamber (Figure 2A). An external circulating chiller and power supply for the heating elements are connected through vacuum portals, and a gas inlet permits controlled introduction of gas into the chamber. To reduce the oxygen content in the chamber before testing, we cyclically evacuate the chamber to ~10^{-2} Torr with a mechanical pump, and backfill with ultra-high purity Ar (99.999%). Testing can be carried out in partial vacuum at ~10^{-2} Torr, or in inert atmospheres by subsequently re-filling the chamber with gas to a desired pressure. In what follows, we use the term "vacuum" to refer to $\leq 10^{-2}$ Torr with the

residual gas atoms being mainly Ar.

We affix samples to the top of the heating cartridge by mechanical clamps (Figure 2B) and measure the sample temperature using a thermocouple attached to the sample surface with high temperature cement. Preliminary trials using the same cement to attach samples to the heater cartridge result in concerns about corrosion of certain samples and the potential for additional compliance; mechanical clamping is employed for all property measurements to avoid these issues. Sample temperature stability better than 0.1^{o} C is attained up to 500^{o} C. In the present design there is no independent heater for the tip. The tip (Figure 2C) is instead heated through thermal transfer from the sample via conduction (during indentation) and convection (when indenting in gas) from the hot sample, as discussed in Ref. [33]. After each indentation, the tip remains in contact with the surface as the stage translates to the next indentation position. Immediately before beginning the indentation, the tip temporarily disengages the surface but remains in close proximity (~100 nm). This sequence is repeated for the remainder of the set, and in this way the tip is cyclically heated and cooled. In-depth discussion of the heat transfer between sample and tip is provided in the context of drift analysis in a subsequent section.

3 System characterization

The accuracy of nanoscale measurements requires dimensional stability in the load column. Thermal expansion or contraction in any portion of the load column results in a moving frame of reference which is usually accounted for as thermal drift and subtracted from the final load-depth response. Thermal drift is measured displacement under a condition when no displacement is

expected to occur, such as under constant loads in non-creeping materials, and is commonly used as a metric of instrument performance. In an appropriately damped system, drift is often negligible at room temperature. At elevated temperatures, however, temperature gradient variation can be more severe and thermal effects such as thermal expansion of the tip and surrounding components are expected to amplify drift, making accurate property measurement more challenging. In our group's prior work on high temperature nanoindentation in air [33], for example, the average drift rate after equilibration increased two orders of magnitude (0.01 to 1 nm s^{-1}) between room temperature and 405^{o} C.

The following drift measurement procedure is used throughout this study. Once the desired sample temperature is reached and stable, the tip is brought into contact with the sample and indentation begins. Drift is measured by monitoring the indenter tip displacement under a constant applied load, for a test material expected to remain rigid given the applied load and contact area (i.e., insignificant creep or viscoelastic deflection). Any displacement measured under such conditions is assumed to be artificial and assigned as drift. We measure the drift at two points in the indentation process: prior to loading at 2 μN for 20 seconds (we term this "preload" drift) and during unloading at 20% of the peak load for 10 seconds (the "unload" drift).

Because it is a typical standard material for calibrating nanoindenters, we use fused silica as a test material. It is grade "N" high-purity manufactured by Tosoh SGM USA (Flemington, NJ) prepared through standard mechanical polishing techniques to better than 2 nm RMS roughness. We measure drift rates in vacuum up to 500^{o} C, which is a low homologous temperature for

fused silica, thus the displacements measured under constant load are taken to arise from drift, and not material creep.

We begin by using a commercial high temperature indenter shaft and tip (Figure 2c) which is composed of a Berkovich diamond tip that is about 20 μm from its tip to its back side, where it is attached by a proprietary high temperature braze to a Macor shaft ~8 mm long. We apply a maximum load of 9.5 mN at a loading and unloading rate of 4 mN s^{-1}. Several identical indentations are performed in succession with 10 μm spacing, and the preload and unload drift rates are measured for each test.

Representative load-displacement curves (with no correction for drift) at various temperatures are shown in Figure 3. The preload drift cannot be seen in these graphs, but the displacement change while holding at 1.9 mN during unloading is apparent (and highlighted by arrows). We define a positive drift as one in which the indenter is apparently moving away from the sample surface, as indicated in Figure 3. At all temperatures, both measured drift rates (preload and unload) are initially transient before reaching a nominally steady state value in $\leq$ 75 minutes from the first contact of cold tip to hot sample (Figure 4).

The two most obvious trends in the drift rate data in Figure 4 are that 1) the unload drift rate increases with temperature while the preload drift rate does not and 2) there is variation in both drift rates with time. (In particular, periodic oscillations are apparent at elevated temperatures, a topic addressed later.) Reducing these trends to the average thermal drift and standard deviation of drift rates provides us two parameters with which to characterize the system throughout this

study. Although the two metrics are not technically independent, each can tell us something unique about the response of the system to testing at elevated temperature. In each case, the statistical quantities are calculated from a minimum of 40 measurements. In what follows, we describe separately the average thermal drift and standard deviation ("noise"), and their respective sources. This discussion then enables us to present strategies for mitigating both.

3.1 Average Thermal Drift

Figure 5A summarizes the average steady state drift rates (e.g. drift at times ≥ 75 minutes in Figure 4) for temperatures up to 500°C. Attention is first directed to two sets of drift measurements for the system baseline under a vacuum atmosphere with a standard tip: preload (labeled "Standard Macor (p)") and unload ("Standard Macor (u)") at each temperature. Though the preload drift rate is small (≤ 0.1 nm s^{-1}) and nominally constant across all temperatures in the tested range, the unloading drift increases monotonically to rates upwards of 1.7 nm s^{-1} at 500°C.

Further testing has shown that the discrepancy between average preload and unload drift rates persists in other sample materials including Cu, Macor, and single crystal 4H-SiC (see Table 1~~Table 1~~). Prior to testing, Cu (99.95% pure) and Macor [50] were mechanically polished to a roughness of 10 nm or better. The SiC (from Cree, Inc., Durham, NC) was furnished with a smooth surface suitable for nanoindentation. These materials were specifically chosen for investigation because of their range of thermal conductivities (1.4 for fused silica [51] to 398 W m^{-1} K^{-1} for Cu [52]) and hardness (0.6 GPa for Cu [52] and 27 GPa for SiC [51]). The unique combinations – for example the higher thermal conductivity and hardness of SiC and the same order of magnitude thermal conductivity but lower hardness of Cu – allow us to understand the

Formatte

contributions of these material properties to drift.

Across the materials tested in this study, preload drift remains at about 0.10 nm s^{-1}, with the exception of Cu, for which we measure 0.25 nm s^{-1}. Comparing these rates to the unloading drift rates in Table 1~~Table 1~~ reveals large deviations among the different materials. In Cu, the unload drift is 150 times that of the preload drift. The unload drift rates increase with the thermal conductivity of the sample materials (Table 1~~Table 1~~): the thermal conductivity of Cu, for example, is nearly 300 times higher than that of fused silica and the unloading drift rate is 30 times higher; the thermal conductivity of SiC is nearly 90 times higher and the unload drift rate is a factor of 5 higher. We note however that these materials have vastly different hardnesses, which alters the contact conditions of the tip. Fused silica and Macor meanwhile have very similar thermal conductivities (1.4 [51] and 1.5 W m^{-1} K^{-1} [50], respectively) and are both of the same order of hardness (5.5 [51] and 2.5 GPa [50], respectively) and the drift rates measured on these two materials are similar.

To understand the difference between the preload and unload drift rates, as well as the trend of the unload drift rate with temperature and material properties (specifically thermal conductivity and hardness), it is helpful to consider the heat transfer situation between sample and tip assembly over the course of a single indentation test. Because the sample is actively heated and the electronics behind the tip are actively cooled, there is the opportunity for thermal transients to develop in the tip assembly over the course of an indentation, leading to thermal expansion of the tip assembly and the measurement of an artificial drift displacement. During an indentation, the tip is cyclically heated and cooled, resulting in thermal expansion of the tip assembly (during

indentation) followed by contraction (in-between indentations). Such thermal expansion is consistent with the directionality of the measured displacements during the unloading hold in Figure 3. In these curves, the observed positive drift displacement nominally represents travel of the indenter tip away from the sample. More accurately, though, this measurement represents an increase in the distance between the transducer and the sample surface. If the tip undergoes thermal expansion under an enforced condition of constant applied load, the transducer responds by retreating from the sample, resulting in the observed displacement. In what follows, we consider the heat transfer situation during indentation, and rationalize in more details drift trends seen in Figure 5 and Table 1~~Table 1~~.

Because the sample and stage are actively heated and are of significant size, they maintain a constant temperature during testing; thermal expansion-related drift is not likely to originate primarily in these components. Similarly, the transducer and the load frame are sufficiently removed from the hot zone that they undergo no thermal expansion over the course of an individual test. Accordingly, the thermal drift in our experiments is believed to come from thermal expansion transients in the tip assembly, which is shown in Figure 2C. Of the components in this assembly, the diamond indenter tip itself is almost certainly *not* responsible for the drift that we measure in our experiments. As noted elsewhere [33], the very high thermal conductivity of diamond suggests that it should be heated quickly and achieve a roughly constant temperature throughout its volume, as long as it is in contact with a hot sample. Second, the displacements we measure in drift are not plausibly ascribed to thermal expansion of diamond: at a test temperature of 300^{o} C the unload drift rate is 1.2 nm s^{-1} (Figure 5A), or 12 nm in total drift displacement over the 10 second measurement time. Even assuming an upper-bound case where

the diamond is at room temperature prior to contact, the displacement due to its thermal expansion would only be ~3 nm (the initial length is 20 μm and linear thermal expansion coefficient 5 x 10^{-7} K^{-1} [53]). We conclude therefore that thermal expansion of the other tip assembly components (indenter shaft and braze) must dominate the drift rate.

For the present conditions, the only important source of heat transfer from the hot sample to the tip assembly is via conduction through the contact point itself; convection plays a negligible role in vacuum conditions, as does radiation for lower test temperatures (below 400º C). At time t = 0, the indenter comes into contact with the sample at higher temperature T_{sample}, and thermal conduction between the two bodies proceeds. The heating of the tip assembly is then responsible for the drift displacement because of thermal expansion. This situation can be modeled to a first approximation as a unidimensional conduction problem involving the joining of two semi-infinite bodies at t = 0. A simple one dimensional solution for this heat transfer problem may be adapted as [54]:

$$\Delta T_{shaft} = \frac{T_{sample}}{1+\left(\frac{D_{shaft}A_{shaft}}{D_{sample}A_c}\right)^{1/2}} erfc\left(\frac{|x|}{2\sqrt{D_{shaft}t}}\right), \quad (1)$$

where ΔT_{shaft} is the temperature increase in the shaft with respect to its initial temperature, which is taken to be ambient temperature, T_{sample} is also relative to ambient temperature, x is the distance along the shaft length, and the thermal diffusivities, D, of the shaft and sample are given by

$$D = \frac{k}{\rho C_p}, \quad (2)$$

where k is thermal conductivity, ρ is density, and C_p is heat capacity.

Because of the rapid thermal conductivity and small dimensions of the diamond tip and the braze that attaches it to the shaft, these components may be neglected entirely as a zero-resistance elements in the balance. However, the indenter tip is geometrically very important: depending upon the applied load and the indentation history, the contact area across which heat may be conducted into the tip assembly from the sample can vary by orders of magnitude. In order to account for this effect, Equation (1) explicitly carries a ratio of two areas: the cross-sectional area of the shaft, A_{shaft} = 3.14 x 10^{-6} m^2, and the indentation contact area, A_c, which is taken to be a function of the indentation contact depth (h_c) based on the geometry of an ideal Berkovich indenter: $A_c = 24.5h_c^2$.

Equation (1) provides the thermal profile in the indenter shaft as a function of time during the indentation; it is straightforward to calculate the expected change in shaft length due to thermal expansion using the linear thermal expansion law with a temperature coefficient of α. The total displacement due to thermal drift (U_{total}) is then found by integrating over the length of the shaft:

$$U_{total} = \int_0^{\infty} \alpha \Delta T_{shaft}(x)dx = \frac{2\alpha T_{sample}\left(\frac{D_{shaft}t}{\pi}\right)^{1/2}}{1+\left(\frac{D_{shaft}A_{shaft}}{D_{sample}A_c}\right)^{1/2}}. \quad (3)$$

Because the present model is extremely simplified, it is not useful for quantitative predictions of drift rates for a given test. However, it does capture all of the major *differential* trends we observe in our experiments: the differences in drift responses between different temperatures, among different samples, and between pre- and unloading conditions. For example, the linear

dependence of drift displacement and drift rate upon sample temperature anticipated by Eq. (3) is indeed seen experimentally (see Figure 5). Similarly, the difference between preload and unload drift rate is captured by the model; Figure 6A displays the preload and unload displacement as a function of time during the hold segment (e.g. constant A_c) in fused silica as calculated by Equation (3) using the correct tip contact areas for those two segments from Table 1~~Table 1~~. The stark difference between unload and preload displacements is similar to our experimental observations (cf. Figure 5), and the quantitative comparison in the inset table to Figure 6A shows that the model properly captures the two order of magnitude difference between preload and unload drift rate. This agreement clarifies the role of contact area in affecting drift; the unloading drift rate is higher because of the increased contact area at the end of the test, permitting more rapid heat transfer into (and associated thermal expansion of) the tip assembly.

The model also captures the large difference in unloading drift between materials. An example of this is shown in Figure 6B, which compares the evolution of drift displacement in Cu and SiO_2; the inset table compares predicted and measured drift rates on all the materials tested for the unload drift measurement. Again, the model properly captures the general trends and orders of the experimental drift rates, and provides insight on the controlling factors. Higher thermal conductivity of the sample and lower hardness (larger contact area) directly inflate the drift rate, by increasing the rate of heat transport into the tip; the scaling in Eq. (3) properly captures these broad trends.

In all cases, the model underestimates drift rates (usually by about a factor of two or three), most likely due to its simple nature. Among other contributing errors, the present calculations may

tend to underestimate the actual contact area through which heat conducts. Pileup of material around the tip, especially in soft materials like Cu, serves to effectively increase the contact area between the tip and hot sample, but is not accounted for in the model. Furthermore, the model assumes a perfect Berkovich tip geometry. In the preloading condition not only is the depth of penetration difficult to know exactly, but the tip is also rounded, resulting in a greater contact area and thus higher measured preload drift rate.

With regards to the extent of heating, we learn from Equation (1) that the transient thermal gradient primarily extends over a distance less than the length of the shaft (8 mm as seen in Figure 2C) for a 10 second measurement time. In fact, even when indenting in a soft, thermally conductive material like Cu, 30 s – which is more than a factor of three larger than the time needed to complete an entire indent sequence – are required for a temperature rise of 1 K at the end of the 8 mm shaft. This point is confirmed experimentally using a tip attached to an even longer Macor indenter shaft (12 mm) where the drift measurements (marked "Extended Macor (u)" in Figure 5A) are found to be nominally the same as those achieved with the standard 8 mm tip assembly. Equations (1-3) have other implications for tip assembly design to reduce drift; we will explore this issue in later sections.

3.2 Noise

The error bars in Figure 5 represent one standard deviation of the data, and provide us with a measure of the scatter in results among nominally identical measurements, hereafter referred to as "noise." High noise indicates high variability in the measured drift rate, which may present obstacles to reliably subtracting thermal drift from the data. Though the noise values are

indicated by the error bars in Figure 5, they are also plotted separately with respect to temperature in Figure 7 to draw attention to their trends, which are unique from the trends in average thermal drift rate. The noise is low and similar in both preload and unload drift measurements up to 400^{o} C; at these temperatures the standard deviation in drift rate is of order 0.1 nm s^{-1}, and we find that this has no measurable effect on the measurement response. From the point of view of data scatter, there is no significant disadvantage of working at elevated temperatures in this range with the present instrument, At 500^{o}C however, the noise abruptly increases by an order of magnitude—a result that we will address in the following section as a special challenge associated with working at T ≥ 500°C.

3.3 Special considerations at T ≥ 500^{o}C

3.3.1 Radiation

As the sample temperature is increased, the thermal radiation emitted from it increases. Above temperatures around 500°C, radiation from the heating cartridge is evident from a visible glow observed through the chamber window. We therefore speculate that the anomalously high noise at 500^{o} C (Figure 7A) is a result of radiated heat interfering with the transducer and electronics. The hole in the actively cooled reflective shield through which the tip assembly passes (Figure 2B) has a larger diameter (4 mm) than that of the tip (2 mm), providing a path for radiation emitted by the sample surface and heater to reach the transducer. Since the intensity of radiation emitted by a body is proportional to T^4, it is reasonable that radiation effects set on suddenly as temperature rises. In a later section, we propose a refinement in the indenter shaft design and provide data that supports our interpretation as regards radiation effects.

Radiated heat interacting with the transducer is also most likely responsible for the periodic oscillations observed in both drift rates at elevated temperatures (Figure 4). It is interesting to note that there are eight data points between a peak and trough in the oscillations, which correlates with the length of one row in the 8x8 grid of indentations used to collect these data. These oscillations are not apparent at room temperature, therefore the effect is not associated with the function of the piezo-electric positioning system alone. Instead, we believe that the correlation with piezo-electric movement derives from the motion of the tip assembly within the through-hole of the cooling shield, changing the amount of "line of sight" radiation that reaches the transducer.

3.4.2 Tip erosion

An additional concern for operation at high temperatures is the effect on the tip material. At temperatures as low as 500°C, there is a potential for diamond to degrade to graphite [55]. Figure 8 shows four representative load-displacement curves – each corrected for drift using unload drift rates recorded for each respective indent — recorded at various temperatures on fused silica. The curves from 23 to 400° C have similar forms; the subtle differences are consistent with the variations of hardness and modulus with temperature. The curve recorded at 500°C, however, exhibits an inflated load at every displacement, culminating in a sharp, oddly shaped peak. This change is found to be permanent, in the sense that load-displacement curves acquired at 23°C after cooling from 500°C are different from the original curve recorded at 23°C. This is not due to any change in the material properties or surface morphology of the test sample, as confirmed by subsequent nanoindentation experiments using a second calibrated tip and instrument not exposed to these temperatures. The permanent change in the load-displacement curve in the

absence of a change in properties indicates a change in the tip geometry. The shape of the distorted load-displacement curve in Figure 8 is consistent with a permanent blunting of the tip, likely caused by accelerated erosion of the diamond at elevated temperatures. Operation of the indenter at 500°C with a second diamond tip confirmed that the apparent blunting occurs readily under these conditions.

The erosion of diamond we observe in the case of indentation on silica in an inert partial vacuum is a general concern for elevated temperature nanoindentation. For other combinations of sample and test atmospheres, the onset of tip erosion and its rate may vary. Sapphire may prove to be a suitable tip material at T >400°C for applications which do not require the extreme hardness of diamond[16, 34]. Until a suitable replacement for diamond is identified, we urge caution in applying nanoindentation at temperatures above 500°C without consideration of this issue.

4 Instrumental and operational refinements

Equipped with the above characterization and understanding of the system, we now examine augmentations to the basic high temperature nanoindentation procedure with the goal of minimizing drift and noise. Because drift arises from thermal expansion, methods for improvement focus on two approaches to minimize the dimensional change of the indenter shaft: (1) reduce expansion-causing thermal gradient fluctuations in the shaft by the addition of a temperature-stabilizing atmosphere and (2) eliminate shaft thermal expansion by appropriate shaft material selection. Additionally, the issue of noise, which is particularly rampant at 500°C, is approached through a minor hardware adaptation.

4.1 Atmospheres

The introduction of a gas atmosphere provides another medium for thermal transport beyond the limiting case of conduction through tip-sample contact in vacuum. Specifically heat can be transferred from the hot sample to the tip assembly (and other system components) through a fluidic medium by conduction, convection, or both.

In these experiments, we measure drift rates as before, but in a chamber back-filled with inert gases—ultra-high purity Ar or He (99.999% pure)—at near atmospheric pressures (~10^2 Torr). The same tip, sample, and loading functions used in the baseline vacuum experiments are maintained for consistency. The preload and unload drift rates measured in these atmospheres are shown along with the baseline measurements in Figure 5B. Also shown for comparison is the unload drift rate obtained in air from the work in Ref. [33]. In all three cases (air, Ar, and He), the average drift rate is reduced as compared with testing in vacuum. Testing in He results in the elimination of the difference between preloading and unloading drift rates. Ar and air do not eliminate this difference entirely, but they are similarly effective at reducing the average unloading drift rate at 300^{o}C. Despite the improved drift rates, however, the noise is three to six times greater than that measured in vacuum (Figure 7B).

The thermal conductivities of air and Ar at 300^{o}C and He at 140^{o}C are 45 [56], 29 [57], and 183 [56] mW $m^{-1}K^{-1}$ respectively, and their efficacies as convective transport agents follow the same trend. Based on such considerations, we can understand why He is particularly effective at heating the system components (and thus eliminating the difference between preload and unload drift rates) and the effectiveness of air and Ar are similar. In fact, we find that He transfers heat

so efficiently that testing above 140°C is not possible with the present apparatus due to unacceptable heating of the transducer. In the lower thermal conductivity gases (air and Ar), testing is performed at 300°C without such problems.

The gas atmosphere acts to stabilize the thermal gradients in the tip assembly against the cyclic heating and cooling caused by the changing tip-sample contact area. The heated gas acts as a heat reservoir that constantly bathes the tip and shaft throughout a set of experiments. As a result, the temperature gradients due to transient thermal conduction from the dynamically changing tip area are made less severe, leading to reduced thermal expansion and the observed reduction in the average thermal drift rate.

4.2 Tip shaft material selection

Reducing thermal drift can also be approached from a materials selection standpoint. If changing thermal gradients are unavoidable, dimensional change in response to temperature variation may still be reduced or avoided by choosing materials with low or zero thermal expansion coefficients. We have investigated an alternative indenter shaft comprising a low thermal expansion material. For these experiments we again return to a vacuum condition, but employ a custom tip assembly manufactured by Hysitron, Inc. (Minneapolis, MN) where the diamond tip is brazed to a shaft made of a near-zero thermal expansion material ($<0.05 \times 10^{-6}$ K^{-1} from 20 to 300^{o}C [58]).

The drift and complementary noise are shown in Figure 5A and Figure 7A, respectively. With this shaft, unload drift is reduced to the low level observed during preloading, while the noise is

similar to that when indenting in vacuum. This trend is in line with expectations based on the heat transfer model described earlier; introducing the thermal conductivity and thermal expansion coefficient of the new shaft material into the model yields a two order of magnitude reduction in drift rate as compared with the Macor shaft. This result provides a final convincing point of evidence that drift in the present instrument is dominated by transient thermal gradients in the indenter shaft. This experiment also demonstrates that tip architecture can materially affect drift response, and indeed should be considered a key element for future design efforts in high temperature nanoindentation.

It is interesting to note that drift, though substantially reduced, is not entirely eliminated by exchanging the shaft material. The diamond tip and braze material are still susceptible to thermal expansion, resulting in the occasional differences between preloading and unloading drift rates, particularly in cases where, because of high thermal conductivity and/or soft materials, a large amount of heat is transferred into the tip from the sample. For example, the average unload drift rate in copper at 300°C is dramatically reduced when using the zero thermal expansion tip architecture (5.6 nm s^{-1} compared to 36.7 nm s^{-1} using a tip attached to a Macor shaft), but it does not reach the preloading drift rate of 0.1 nm s^{-1}.

4.3 Radiation management

As noted above, noise becomes particularly problematic at 500°C, (cf. Figure 7), due to a presumed influence of radiative heating between sample and transducer. More specifically, the line-of-sight radiation pathways between sample and transducer through the center tip-hole in the actively cooled shield (Figure 2) allow heating of the transducer. To verify this speculation, and

to mitigate such radiative heating, an additional reflection shield is added to the tip assembly. A polished Cu skirt 5 mm in diameter (0.5 mm thick) is attached around the tip shaft between the shield and the transducer ~~(Figure 2B)~~. With its high reflectivity, polished copper deflects incoming radiation passing through the hole in the shield from directly reaching the transducer. The average unloading drift (Figure 5A) remains nominally the same for a tip with a Macor shaft and this secondary shield, but this addition successfully reduces the noise by a factor of three (Figure 7A).

5 Property measurements

Having gained an understanding of thermal transport in the system and the optimum hardware and procedural adaptations required to control drift and noise, we turn our attention to validation of the instrument through the measurement of hardness and modulus of three materials: fused silica, aluminum, and copper. For all of the tests in this section we use a zero thermal expansion shaft. Sufficiently low drift rates are maintained using a vacuum atmosphere for indentation in fused silica, while the additional drift suppression from an Ar atmosphere at ~10^2 Torr is necessary for indentation of Al and Cu, owing to their higher thermal conductivities (Table 1~~Table 1~~). To further mitigate the higher drift rates in Al and Cu, we limit the tip-sample contact area by restricting the maximum peak load to 4 and 2 mN, respectively. Additional testing details for all three materials are summarized in Table 2. As a consequence of these testing conditions, the total drift that occurs from the start of the indentation to 20% unload is estimated at $\leq$ 2.1 nm in all materials at all testing temperatures. Such a small total drift causes a change of < 5% in the extracted hardness and modulus values, which is lower than the uncertainty on these values even in normal room temperature operation.

Formatte

Several load-displacement curves are recorded for each sample material at temperatures ranging up to the maximum testing temperatures listed in Table 2. Only indentations recorded after the initial transient period in average drift rate (as exhibited in Figure 4) are considered, which amounted to 20 or more indentations for each sample material and condition. Drift correction is applied to each load-displacement curve using the unload drift rate measured for that curve.

Machine compliance is calibrated at temperatures from 23 to 400°C. The compliance increases from 0.7 nm mN^{-1} at 23°C to 1.2 nm mN^{-1} at 100°C and then remains constant up to 400°C. We use this temperature-dependent compliance in our subsequent property extraction using the Oliver-Pharr method [59] and a tip area function calibrated at room temperature [33].

5.1 Fused silica

The fused silica is the same as that used for tests described in previous sections: grade "N" high-purity manufactured by Tosoh SGM USA (Flemington, NJ) and prepared to better than 2 nm RMS roughness.

Figure 9 shows the measured hardness and modulus of fused silica as a function of temperature. Each data point represents the average of more than 50 indentations with the error bars showing one standard deviation. The average unload drift rate is ≤ 0.3 nm s^{-1} at temperatures up to and including 400°C. The present hardness results (Figure 9A) show a softening of silica with increased temperature and have good agreement with similar nanoindentation data collected in air [24, 33]. Modulus results (shown in Figure 9B) also match literature trends for fused silica,

which shows stiffening with increased temperature, an anomalous trend which sets silica apart from many other materials. The present data, which align well with the results of Ref. [33], also agree with acoustic measurements of the modulus of fused silica [60-63] compiled in Ref. [33].

An important point from Figure 9 is that the present standard deviations for hardness and modulus (Figure 9) of fused silica in vacuum are smaller than those reported in the literature using a similar indentation apparatus in air. For example, at 300°C, the standard deviation in Schuh and coworkers' [33] hardness data is ±0.22 GPa while we record a standard deviation of ±0.06 GPa on a similar sample size. This comparison validates that a consequence of reducing drift rate–by operating in vacuum in this case–is enhancement of the precision of property measurements.

5.2 Aluminum

Aluminum (99.998% pure) from Alfa Aesar (Ward Hill, MA) is annealed at 500°C in a box furnace for 36 hours to pre-coarsen the structure and minimize grain growth during testing. To remove oxide that forms during annealing and prepare a smooth surface for nanoindentation, we grind, polish and etch it (80% H_3PO_4, 15% H_2SO_4, and 5% HNO_3 by volume) for 4-5 minutes at 95°C [64]; the as-tested roughness is about 10 nm.

At test temperatures that are a significant fraction of a material's melting temperature, displacement may result from creep as well as thermal drift, and discerning the difference becomes a problem. Accordingly, to limit the scope of the present work to the non-creeping regime, for our indentations on aluminum the maximum testing temperature is restricted to

100°C, or 0.4 T/T_m where T_m is the melting temperature of Al; for such conditions the displacement during the unloading hold can be attributed to thermal drift alone [65].

Property data was extracted from 20 indentations each at 23 and 100°C. To minimize drift the tests were conducted in ~10^2 Torr Ar and in combination with the chosen test loads and durations (Table 2), the total drift was maintained below 1.8 nm. The average hardness and modulus of the aluminum at 23 and 100°C are shown in Figure 10 with error bars representing the standard deviation. The hardness decreases with temperature as expected for a crystalline metal (Figure 10A) [52]. For comparison, temperature dependent hardness data extracted from several studies of high purity (>99%) aluminum are also presented [23, 48, 66-67]. The vertical positions of these various datasets are all somewhat different, which is expected based on different sample purity, indentation rates, dislocation contents, grain sizes, indentation sizes, etc. More important than the exact position of the data in this figure are their slopes; all data show temperature-induced softening behavior, and dH/dT is quite consistent among these studies, ranging only from -0.7 to -1.2 MPa K^{-1}. Here we measure dH/dT = -0.8 MPa K^{-1} which is within the range of literature values. However, we note that of the data in Figure 10A, most are from conventional microscale hardness indentations and not nanoindentation. The only other nanoindentation study of Al at elevated temperatures was done by Kraft and coworkers [23] on a single crystal, in an air atmosphere. They recorded the hardness at temperatures from 25 to 100°C and strain rates from 0.002 s^{-1} to 0.04 s^{-1}. In their study, dH/dT ranged from -0.7 MPa K^{-1} to -1.2 MPa K^{-1} and had no relation with strain rate. Again, our results (-0.8 MPa K^{-1}) fall within this range.

Although hot hardness values for aluminum are reported in literature, corresponding modulus

data are apparently not available. However, temperature-dependent elastic properties for >99.9% pure single-crystal Al have been measured by acoustic methods [68-73]. To directly compare these literature values to the reduced modulus recorded here, we calculate the temperature dependent reduced modulus of Al by

$$\frac{1}{E_r} = \left(\frac{1-\nu_d^2}{E_d}\right) + \left(\frac{1-\nu_s^2}{E_s}\right) \quad (5)$$

where E is the Young's modulus, ν is the Poisson's ratio, and subscripts d and s refer to the properties of diamond and the sample material (in this case Al), respectively. For accuracy, we use both a temperature dependent ν_s (values for which are also taken from literature [68-73]) and $E_{d,}$ which is equal to [74]

$$E_d = E_d^{RT}[1 + c(T - 293)] \quad (6)$$

where the superscript RT denotes the room temperature modulus of diamond (~150 GPa [53]) and c is an empirical constant (-1.027 x 10^{-4} K^{-1}). Because ν_d is usually well-approximated as temperature independent, we use 0.07 [53].

The reduced modulus calculated from the acoustic data of Ref. [68-73] are compared with the present measurements in Figure 10B. The present measurements are reasonably close to the single crystal data at room temperature, and only marginally below at 100º C; the deviation is within the uncertainty range normally placed on modulus measurements by nanoindentation (±20%) and about one standard deviation in the measurements. The small difference may be due

to crystal orientation or multiaxiality, which is known to cause changes of such order in the reduced modulus measurement [75]. Most encouraging is the trend of decreasing modulus with temperature in the nanoindentation measurements. What is more, after indentation, the sample surface is visually identical to its condition before testing, as expected for our inert test conditions.

5.3 Copper

Copper (99.95% pure, Online Metals, Seattle, WA) is mechanically polished to prepare a smooth surface for nanoindentation. The sample is then annealed at 425°C in the nanoindentation vacuum chamber at ~10^{-2} Torr for 20 hours in order to pre-coarsen the structure and minimize grain growth during subsequent testing. Indentation data is recorded at temperatures from 23 to 400°C in ~10^{2} Torr Ar after equilibration of the instrument at each temperature. The average drift rate increases with temperature, reaching a maximum of 2.3 nm s^{-1}, but as in the case of Al, the total drift is low (2.1 nm) because of the low maximum load (2.0 mN) and short duration of the experiments (Table 2).

Figure 11 shows the average hardness and modulus of 20 indentations, with error bars representing the standard deviations. Nanoindentation of Cu at temperatures up to 200°C has previously been reported by our group [37] but this is the first report, to our knowledge, of nanoindentation of Cu up to 400°C. The hardness (Figure 11A) decreases with increasing temperature, similar in trend to hot microhardness taken from numerous studies of >99% pure Cu [66-67, 76-79]. The slopes dH/dT for these hot microhardness studies range from -0.4 to -1.1 MPa K^{-1} with an average of -0.7 MPa K^{-1}. The dH/dT measured here (-0.9 MPa K^{-1}) falls within the

range and close to the average.

The reduced modulus of Cu as a function of temperature as measured by nanoindentation is shown in Figure 11B. With no prior nanoindentation data to compare with, here we again calculate reduced modulus values from acoustic measurements taken on pure single-crystal Cu [68, 70, 80-86]. Both sets of data show a decrease in reduced modulus with temperature and match to within experimental errors and uncertainties; the slope of the data is -0.04 GPa K^{-1}.

In both Al and Cu, the standard deviations in hardness and modulus at elevated temperatures are larger than those attained in fused silica. This is a consequence of using an Ar gas environment to reduce the average drift rate, and is reflective of the increased measurement noise in such conditions as shown in **Error! Reference source not found.**~~Figure 6~~. Nevertheless, the results from Al and Cu highlight one of the greatest utilities of this instrument: the ability to extract hardness and modulus data on oxidizing materials on small scales at elevated temperature in an inert atmosphere.

6 Summary and implications

We have adapted a commercial nanoindentation instrument to operate at elevated temperatures in inert atmospheres, including vacuum as well as Ar and He gases. The drift rate and noise, which are measures of the ability to accurately and reliably achieve artifact-free data, are characterized for different atmospheres, tip architectures, and testing materials.

When a standard high temperature tip with a Macor shaft is used, drift rates increase with temperature due to cyclical thermal expansion of the tip assembly in vacuum. Besides the thermal expansion coefficient of the shaft material, two other variables affecting the drift rate are thermal conductivity of the sample and contact area between the tip and sample. A higher sample thermal conductivity causes a steeper thermal gradient across the tip assembly, increasing thermal expansion drift. And because heat is primarily transferred through conduction in these tests, drift rate is dependent on the size of the conductive path between sample and tip, i.e., the indentation contact area.

Drift rates are reduced by operating in a gaseous atmosphere, because the gas stabilizes the temperature profile of the tip assembly by providing additional heat transport paths between sample and tip. There is a trade-off of drift for noise, however, as noise increases when testing in a gas atmosphere as compared to in vacuum. Additionally, the average drift rate can be reduced by using a tip with a zero thermal expansion shaft, which does not respond to the changing thermal gradients that normally result in drift.

At temperatures approaching 500°C, additional issues emerge. Radiation emitted by the hot sample begins to interact with the transducer resulting in a dramatic increase in noise; this may be mitigated to some extent by adding additional reflectors in the tip assembly. Also, beginning at about 500^{o}C, erosion of the diamond tip is not only observed, but has a marked influence on the measured load-displacement response. The design of future tips for higher temperature nanoindentation will have to incorporate novel materials for the tip to avoid such a change in area – a critical parameter for measuring hardness.

Indentation in fused silica, aluminum, and copper at elevated temperatures up to 400^{o}C and comparison of the extracted mechanical properties to established literature values are used to verify the performance of the instrument and reliability of the technique. For all cases, the hardness and modulus trends and magnitudes are similar to literature values, although these are in each case the first nanoindentation data acquired at elevated temperatures in inert atmospheres. In cases where prior hot nanoindentation data in air are available, we observe improved precision by virtue of operating in controlled atmosphere.

Adding an elevated temperature capability to nanoindentation is the next logical progression for an already powerful technique. As the nanoindentation community pushes the technique to new regimes of scale and temperature, however, it will be necessary for the standards community to compile best practices, including recommendations or requirements for drift rates, calibration procedures, and oxidation limits. With the appropriate understanding of the barriers, many of which are described and characterized in this paper, such practices can begin to be identified. Through our validation experiments, we highlight one of the best utilities of this instrument: the ability to indent materials that readily oxidize, such as Al and Cu, at elevated temperatures on the nanoscale. While previous hot hardness of metals have been reported, typical approaches either involved using a large scale indent (to avoid effects from any oxide that may form and grow) or limiting the study to those materials that do not readily oxidize. With the instrumentation and techniques presented here, such compromise is unnecessary.

Acknowledgements—The authors acknowledge collaboration with Hysitron, Inc., who provided

expertise, instrumentation, and support for this work. In particular, the efforts of Thomas Wyrobek, Fred Tsuchiya, and Oden Warren are gratefully acknowledged. Partial support of the US Office of Naval Research, under contract No. N00014-08-1-0312, and the US Army through the Institute for Soldier Nanotechnologies at MIT, are also acknowledged.

Table 1: Sample materials indented at 300°C and the measured unload drift rates. The drift rate increases with the thermal conductivity of the sample material.

Sample Material	Thermal conductivity ($W\ m^{-1}\ K^{-1}$)	Contact area during unload hold (m^2)	Measured unload drift rate ($nm\ s^{-1}$)
Fused silica	1.4 [51]	7.1×10^{-13}	1.2 ± 0.1
Macor	1.5 [50]	9.8×10^{-13}	1.5 ± 0.2
4H-SiC	120 [51]	6.1×10^{-14}	5.6 ± 0.2
Copper	398 [52]	1.9×10^{-12}	36.7 ± 3.6

Table 2: Loading conditions and unload drift rates for measurements of material properties.

Sample material	Max. test temperature T_{max} (^{o}C)	Max. depth (nm)	Max. load (mN)	Loading rate (mN s^{-1})	Avg. drift rate at T_{max} (nm s^{-1})	Total drift at T_{max} (nm)
Fused SiO_2	400	290	10.0	4.0	0.3	1.4
Al	100	620	4.0	4.0	1.0	1.8
Cu	400	320	2.0	4.0	2.3	2.1

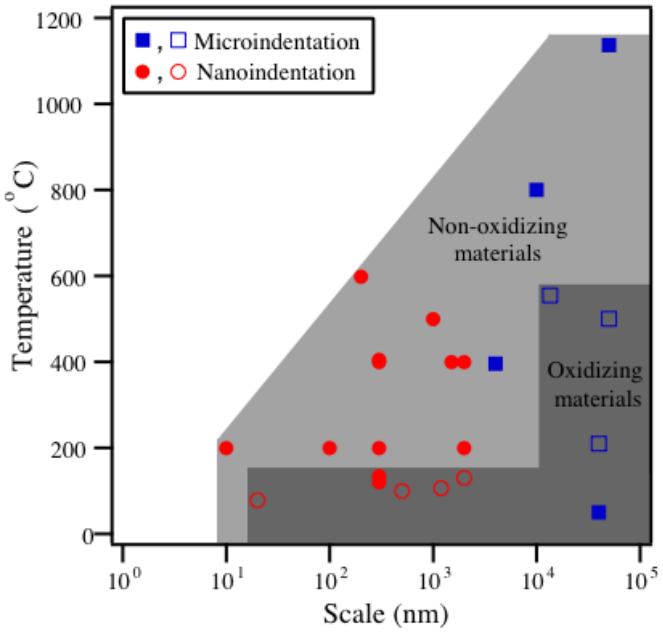

Figure 1: The interplay between temperature and indentation scale established by previous nano- and micro-indentation (differentiated with circles and squares, respectively) at elevated temperatures [3, 5, 8, 10-46]. Two regions are identified: one that is defined by indentation on non-oxidizing materials and a second, much smaller regime that is defined by metals alone (open symbols). To expand the second regime, minimization of thermal drift and sample oxidation are required.

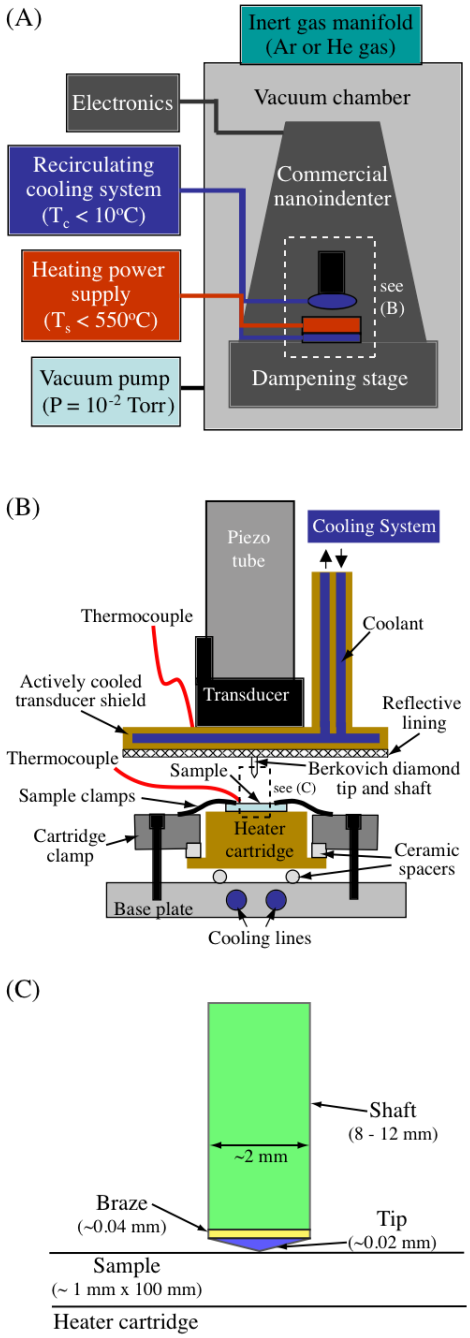

Figure 2: Schematic of (A) the nanoindenter integrated with the vacuum chamber and heating and cooling systems. (B) is an expanded view of the dashed box in (A) which includes the indenter assembly (e.g. piezo tube and transducer), actively cooled transducer shield, and the heater cartridge. (C) is a schematic of the tip engaged with the sample (highlighted by the dashed box in (B)) and its dimensions.

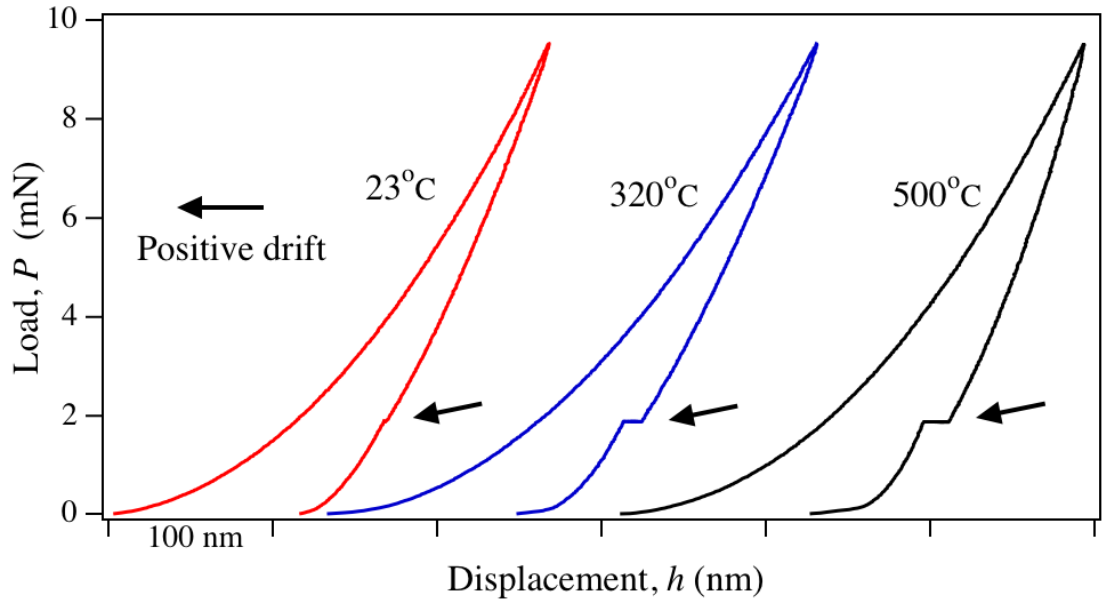

Figure 3: Representative load-displacement curves recorded on fused silica at 23, 320, and 500°C in vacuum with a Berkovich diamond tip attached to a standard Macor shaft. The unload drift is measured by holding at load *P*=1.9 mN during unloading for 10 seconds. The recorded displacement (indicated by arrows) is the drift, which increases with temperature. The larger arrow indicates the direction we define as positive drift.

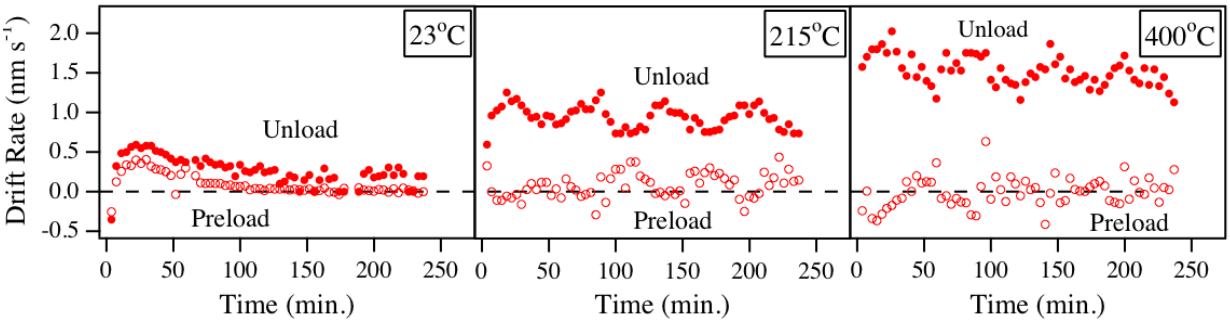

Figure 4: Drift rates measured during preloading and unloading as a function of indentation time. Each point on the graphs is taken from a single indentation.

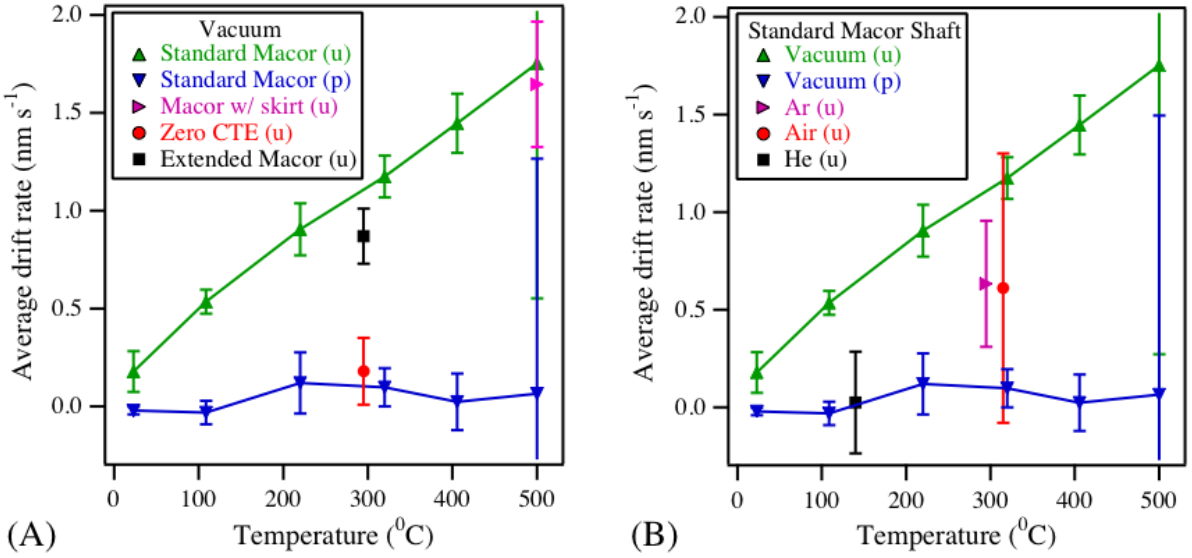

Figure 5: Average steady state drift rates as a function of temperature measured using (A) different tip architectures in vacuum and (B) in different inert atmospheres using a tip with a standard Macor shaft (without a secondary shield). The error bars represent one standard deviation. The "(u)" and "(p)" demarcations next to each data label indicate whether the drift rate is unload or preload, respectively. Data for "Air" in (B) are extracted from Ref. [33].

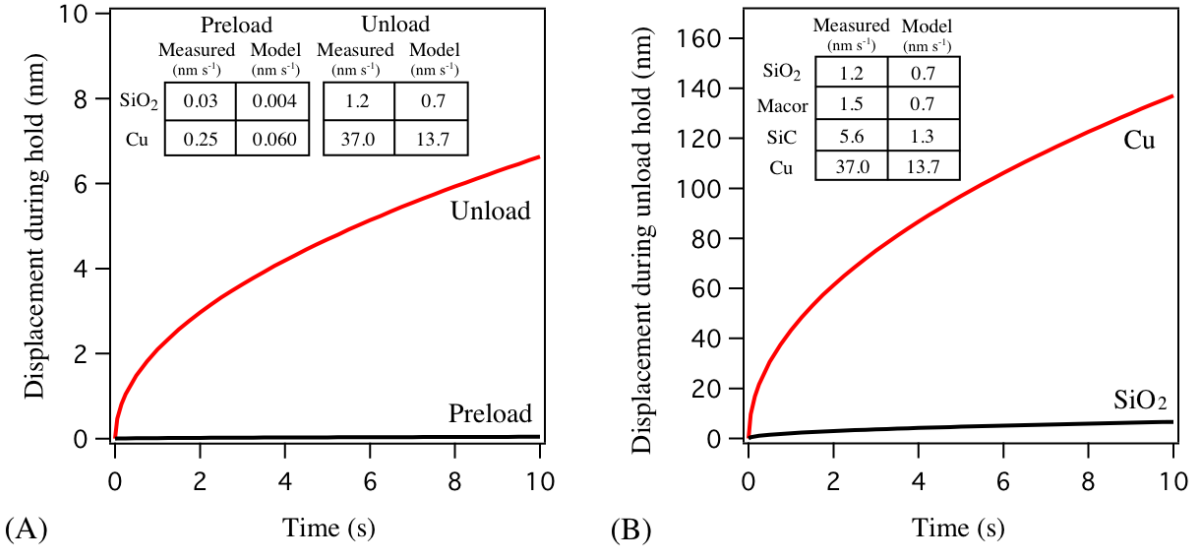

Figure 6: Displacement as a function of time of a tip assembly (diamond tip with a Macor shaft) during unload and preload holds in several materials as calculated by the model presented here. (A) The calculated displacements during a preload and unload hold in fused silica. The inset table displays the measured and calculated preload and unload drift rates for comparison in both fused silica and Cu. (B) The calculated displacements during an unload hold in fused silica and Cu. The inset table displays the measured and calculated unload drift rates for several materials tested.

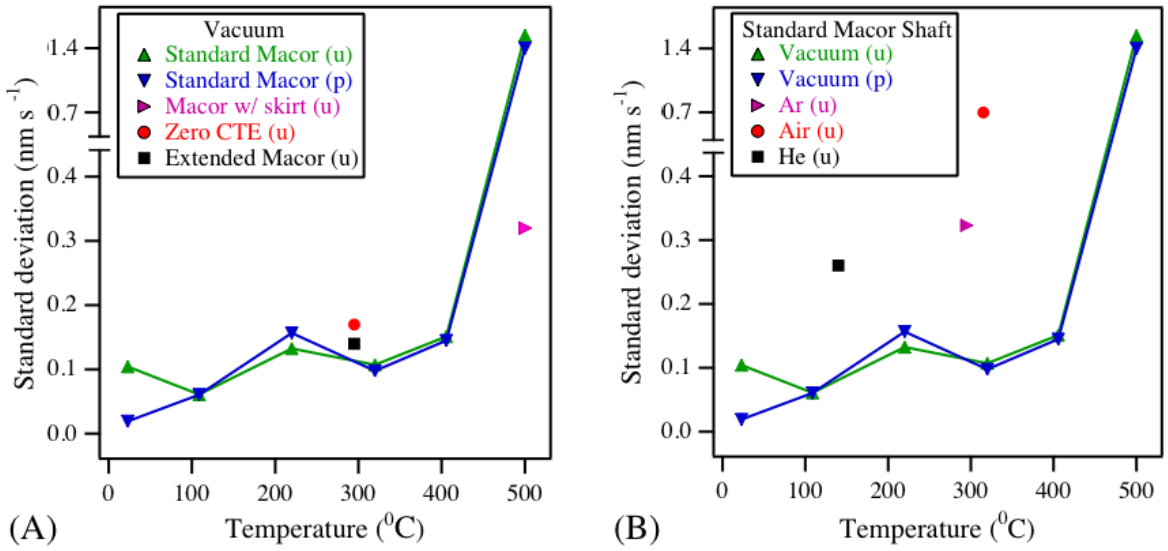

Figure 7: Noise (standard deviation of the average drift rates) as a function of temperature (A) using different tip architectures in vacuum and (B) using a tip with a Macor shaft in different inert atmospheres. The "(u)" and "(p)" demarcations next to each data label indicate whether the noise is related to the unload or preload drift rate, respectively. Data for "Air" in (B) are extracted from Ref. [33].

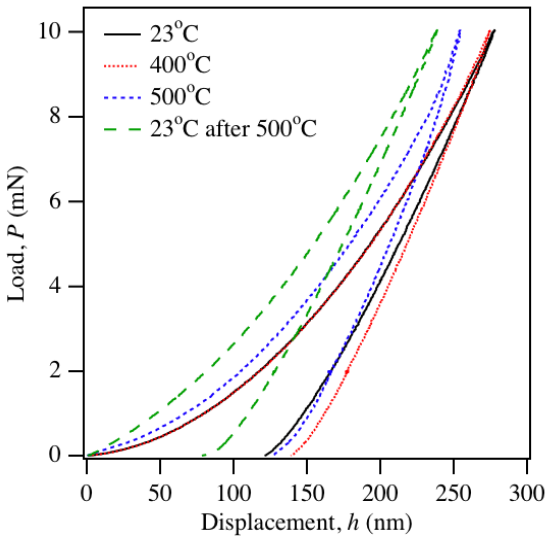

Figure 8: Load-displacement curves (corrected for drift using unloading drift) recorded in fused silica at various temperatures using a diamond tip attached to a zero thermal expansion shaft. Indentations recorded at 23 and 400°C are consistent with the changes in hardness and reduced modulus. A significant change in the shape of the curve is observed at 500°C, and this change persists after cooling to 23° C again.

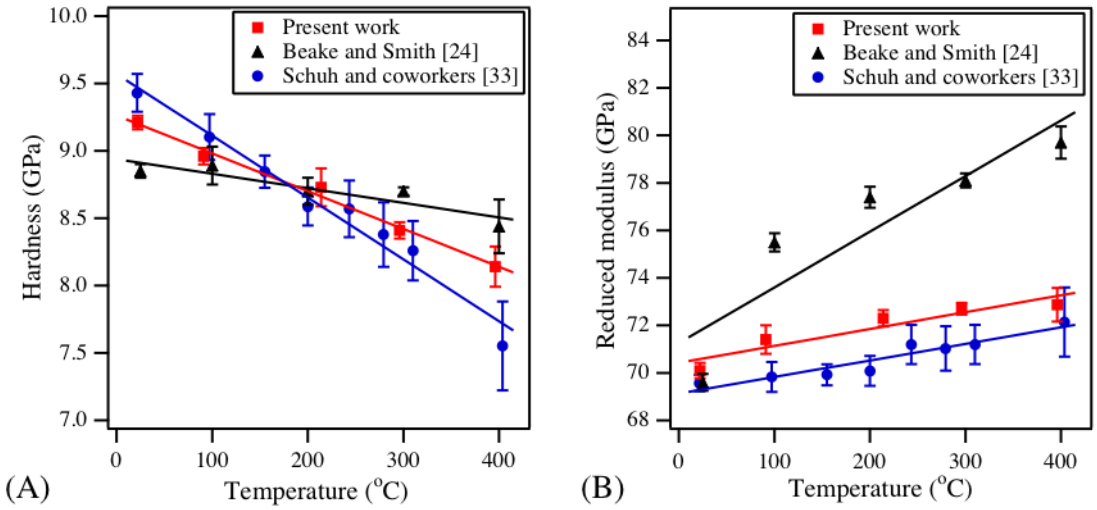

Figure 9: (A) Hardness and (B) reduced modulus of fused silica as a function of temperature measured by nanoindentation. For the present work, measurements were done in vacuum with a diamond tip attached to a zero thermal expansion shaft. Each data point represents more than 50 indentations each with the error bars being the standard deviations of those averages. For comparison, similar data recorded in air by Schuh and coworkers [33] and Beake and Smith [24] are also shown.

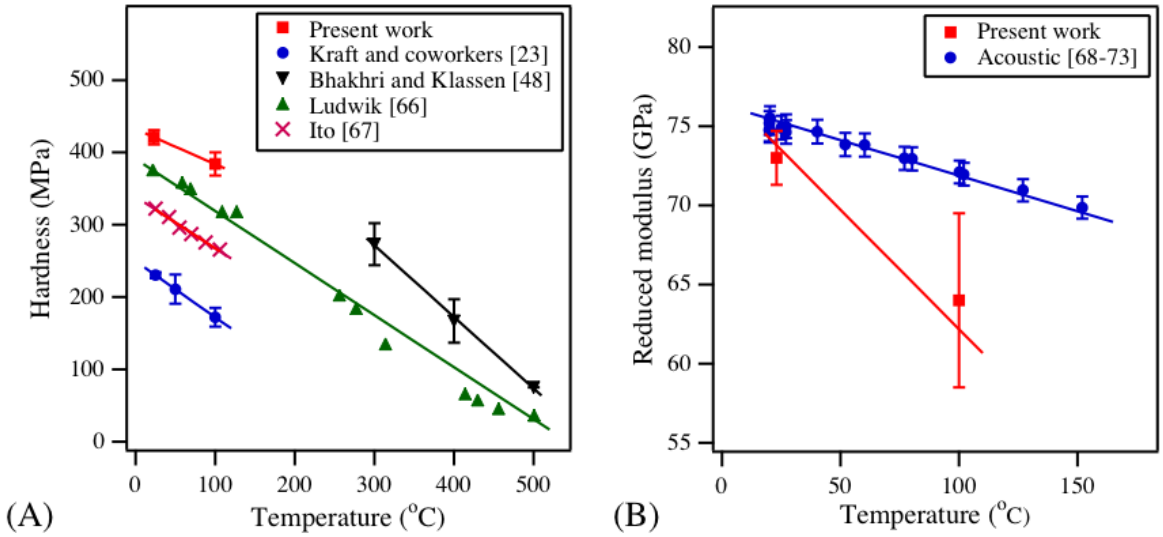

Figure 10: (A) Hardness and (B) reduced modulus of annealed Al (99.998% pure) as a function of temperature measured by nanoindentation. For the present work, measurements were done in Ar near atmospheric pressure with a diamond tip attached to a zero thermal expansion shaft. Each data point represents the average of more than 20 indentations each with the error bars being the standard deviations of those averages. For comparison, hardness values collected using nanoindentation [23] and hot microhardness [48, 66-67] are also shown in (A). Reduced modulus data in (B) is compared to that calculated from acoustic data [68-73].

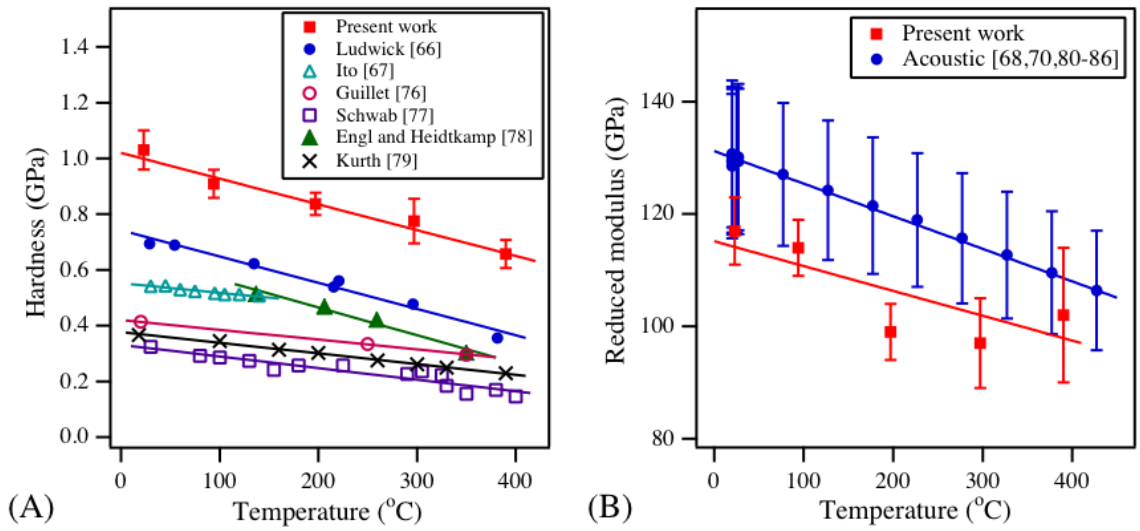

Figure 11: (A) Hardness and (B) reduced modulus of annealed Cu (99.95% pure) as a function of temperature measured by nanoindentation. For the present work, measurements were done in Ar near atmospheric pressure with a diamond tip attached to a zero thermal expansion shaft. Each data point represents the average of more than 20 indentations each with the error bars being the standard deviations of those averages. Hardness values in (A) are compared to hot hardness data [66-67, 76-79] while reduced modulus values in (B) are compared to that calculated from acoustic data [68, 70, 80-86].

1. A. C. Fischer-Cripps, *Nanoindentation*. (Springer, New York, 2002).

2. J. K. Mason, A. C. Lund and C. A. Schuh, Phys. Rev. B **73** , 054102 (2006).

3. D. F. Bahr, D. E. Wilson and D. A. Crowson, J. Mater. Res. **14** , 2269 (1999).

4. C. A. Schuh and A. C. Lund, J. Mater. Res. **19**, 2152 (2004).

5. C. A. Schuh, A. C. Lund and T. G. Nieh, Acta Mater. **52** , 5879 (2004).

6. C. E. Packard and C. A. Schuh, Acta Mater. **55** , 5348 (2007).

7. J. I. Jang, M. J. Lance, S. Q. Wen, T. Y. Tsui and G. M. Pharr, Acta Mater. **53** , 1759 (2005).

8. X. G. Ma and K. Komvopoulos, J. Mater. Res. **20** , 1808 (2005).

9. Y. J. Zhang, Y. T. Cheng and D. S. Grummon, J. Appl. Phys. **98** , 033505 (2005).

10. B. N. Lucas and W. C. Oliver, in *Thin Films: Stresses and Mechanical Properties V*, edited by S.P. Baker, C.A. Ross, P.H. Townsend, C.A. Volkert, and P. Borgesen (Mater. Res. Soc. Symp. Proc. **356**, Pittsburgh, PA, 1995).

11. B. Y. Farber, V. I. Orlov and A. H. Heuer, Phys. Status Solidi A **166** , 115 (1998).

12. B. Y. Farber, V. I. Orlov, V. I. Nikitenko and A. H. Heuer, Phil. Mag. A **78** , 671 (1998).

13. B. N. Lucas and W. C. Oliver, Metall. Mater. Trans. A **30** , 601 (1999).

14. M. Fujiwara and M. Otsuka, Mater. Sci. Eng. A **319**, 929 (2001).

15. H. Takagi, M. Dao, M. Fujiwara and M. Otsuka, Phil. Mag. **83** , 3959 (2003).

16. M. Watanabe, C. Mercer, C. G. Levi and A. G. Evans, Acta Mater. **52** , 1479 (2004).

17. H. Takagi, M. Fujiwara and K. Kakehi, Mater. Sci. Eng. A **387-89**, 348 (2004).

18. S. A. S. Asif and J. B. Pethica, Phil. Mag. A **76** , 1105 (1997).

19. T. Suzuki and T. Ohmura, Phil. Mag. A **74**, 1073 (1996).

20. J. F. Smith and S. Zheng, Surf. Eng. **16**, 143 (2000).

21. B. Wolf, K. O. Bambauer and P. Paufler, Mater. Sci. Eng. A **298**, 284 (2001).

22. D. E. Kramer, K. B. Yoder and W. W. Gerberich, Phil. Mag. A **81**, 2033 (2001).

23. O. Kraft, D. Saxa, M. Haag and A. Wanner, Z. Metallkde. **92** (9), 1068-1073 (2001).

24. B. D. Beake and J. F. Smith, Phil. Mag. A **82** , 2179 (2002).

25. B. D. Beake, S. R. Goodes and J. F. Smith, Z.Metallkde. **94** , 798 (2003).

26. J. Xia, C. X. Li and H. Dong, Mater. Sci. Eng. A **354**, 112 (2003).

27. A. A. Volinsky, N. R. Moody and W. W. Gerberich, J. Mater. Res. **19**, 2650 (2004).

28. M. Hinz, A. Kleiner, S. Hild, O. Marti, U. Durig, B. Gotsmann, U. Drechsler, T. R. Albrecht and P. Vettiger, Eur. Polym. J. **40** , 957 (2004).

29. A. C. Lund, A. M. Hodge and C. A. Schuh, Appl. Phys. Lett. **85** , 1362 (2004).

30. T. G. Nieh, C. Iwamoto, Y. Ikuhara, K. W. Lee and Y. W. Chung, Intermetall. **12**, 1183 (2004).

31. C. A. Schuh, J. K. Mason and A. C. Lund, Nat. Mater. **4** , 617 (2005).

32. Y. J. Zhang, Y. T. Cheng and D. S. Grummon, J. Appl. Phys. **98** , 4 (2005).

33. C. A. Schuh, C. E. Packard and A. C. Lund, J. Mater. Res. **21**, 725 (2006).

34. A. Sawant and S. Tin, Scripta Mater. **58**, 275 (2008).

35. V. Domnich, Y. Aratyn, W. M. Kriven and Y. Gogotsi, Rev. Adv. Mater. Sci. **17**, 33 (2008).

36. K. I. Park, J. H. Kim, H. K. Lee and D. K. Kim, Mod. Phys. Lett. B **23**, 3877 (2009).

37. O. Franke, J. C. Trenkle and C. A. Schuh, submitted for review (2010).

38. D. C. Jones, Y. C. Lu, C. P. Tandon, S. Putthanarat and G. A. Schoeppner, presented at 2008 ASME Internation Mechanical Engineering Congress and Exposition (American Society of Mechanical Engineers, Boston, MA, 2008).

39. K. V. Rajulapati, M. M. Biener, J. Biener and A. M. Hodge, Phil. Mag. Lett. **90**, 35 (2010).

40. Y. D. Han, H. Y. Jing, S. M. L. Nai, L. Y. Xu, C. M. Tan and J. Wei, J. Electron Mater. **39**, 223 (2010).

41. C. L. Wang, M. Zhang and T. G. Nieh, J. Phys. D **42**, 115405 (2009).

42. C. L. Wang, Y. H. Lai, J. C. Huang and T. G. Nieh, Scripta Mater. **62**, 175 (2010).

43. C. E. Packard, J. Schroers and C. A. Schuh, Scripta Mater. **60** , 1145 (2009).

44. F. Gao, H. Nishikawa, T. Takemoto and J. Qu, Microelectron. Reliab. **49**, 296 (2009).

45. J. R. Trelewicz and C. A. Schuh, Scripta Mater. **61**, 1056 (2009).

46. M. Rathinam, R. Thillaigovindan and P. Paramasivam, J. Mech. Sci. Technol. **23**, 2652 (2009).

47. Z. C. Duan and A. M. Hodge, JOM **61**, 32 (2009).

48. V. Bhakhri and R. J. Klassen, J. Mater. Sci. **41**, 2259 (2006).

49. V. Bhakhri and R. J. Klassen, J. Mater. Sci. **41**, 2249 (2006).

50. CORNING, Technical Data Sheet, Macor, Corning, Inc., Corning, N.Y.

51. *Concise Encyclopedia of Advance Ceramic Materials*, edited by R. J. Brook, (Perganon Press, Oxford, 1991).

52. *Smithells Metals Reference Book*, edited by W. F. Gale and T. C. Totemeier, (Elsevier Butterworth-Heinemann, Boston, 2004).

53. *Materials Handbook: A Concise Desktop Reference*, edited by F. Carderelli, (Springer, London, 2008).

54. J. Crank, *The Mathematics of Diffusion*. (Clarendon Press, Oxford, 1979).

55. H. O. Pierson, *Handbook of Carbon, Graphite, Diamond, and Fullerenes*. (Noyes, Publications, Park Ridge, 1993).

56. J. R. Welty, C. E. Wicks, R. E. Wilson and G. Rorrer, *Fundamentals of Momentum, Heat, and Mass Transfer*. (John Wiley & Sons, New York, 2001).

57. A. J. Rothman and L. A. Bromley, Ind. Eng. Chem., 899 (1955).

58. SCHOTT, Technical data sheet, Zerodur, SCHOTT, Inc., Elmsford, N.Y.

59. W. C. Oliver and G. M. Pharr, J. Mater. Res. **7**, 1564 (1992).

60. N. Shinkai, R. C. Bradt and G. E. Rindone, J. Am. Ceram. Soc. **64**, 426 (1981).

61. J. W. Marx and J. M. Sivertsen, J. Appl. Phys. **24**, 81 (1953).

62. S. Spinner and G. W. Cleek, J. Appl. Phys. **31**, 1407 (1960).

63. J. A. Bucaro and H. D. Dardy, J. Appl. Phys. **45**, 5324 (1974).

64. *Metallography and Microstructures*, edited by G. F. Vander Voort, (ASM International, Materials Park, OH, 2004).

65. M. F. Ashby, Acta Metall. Mater. **20**, 887 (1972).

66. P. Ludwik, Z. Phys. Chem. **91**, 232 (1916).

67. K. Ito, Sci. Rep. Tohoku Imperial University **12**, 137 (1923).

68. K. S. Alexandrov and T. V. Ryzhova, Sov. Phys. - Cryst. **6**, 228 (1961).

69. D. Gerlich and E. S. Fisher, J. Phys. Chem. Solids **30**, 1197 (1969).

70. R. F. S. Hearmon, Rev. Mod. Phys. **18**, 409 (1946).

71. P. M. Sutton, Phys. Rev. **91**, 816 (1953).

72. J. F. Thomas Jr., Phys. Rev. **175**, 955 (1968).

73. J. Vallin, J.Appl. Phys. **35**, 1825 (1964).

74. F. Szuecs, M. Werner, R. S. Sussmann, C. S. J. Pickles and H. J. Fecht, J. Appl. Phys. **86**, 6010 (1999).

75. A. K. Bhattacharya and W. D. Nix, Int. J. Solids Struct. **24**, 881 (1988).

76. L. Guillet, Rev. Metall. **21**, 295 (1924).

77. G. M. Schwab, T. Faraday Soc. **45** (4), 385 (1949).

78. J. Engl and G. Heidtkamp, Z.Phys. **95**, 30 (1935).

79. A. Kurth, Z. Ver Dtsch. Ing. **53**, 85 (1909).

80. Y. A. Chang, J. Appl. Phys. **37**, 3567 (1966).

81. S. G. Epstein and O. N. Carlson, Acta Metall. Mater. **13**, 487 (1965).

82. Y. Hiki and A. Granato, Phys. Rev. **144**, 411 (1966).

83. D. Lazarus, Phys.Rev. **76**, 545 (1949).

84. W. C. Overton Jr. and J. Gaffney, Phys. Rev. **98**, 969 (1955).

85. R. E. Schmunk and C. S. Smith, Acta Metall. Mater. **8**, 396 (1960).

86. K. D. Swartz and A. V. Granato, J.Acous. Soc. Am. **38**, 824 (1965).